construction materials

MDPI

Article

Experimental Study on the Drying Shrinkage Behavior of Fiber-Reinforced Normal and High-Strength Concrete Under Different Ambient Conditions

Tamim A. Samman, Khatib Zada Farhan and Md Ashraful Hossain *

Civil and Environmental Engineering Department, Faculty of Engineering, King Abdulaziz University, Jeddah 21589, Saudi Arabia; tasamman@kau.edu.sa (T.A.S.); khatibfarhankau@gmail.com (K.Z.F.)
* Correspondence: ashraful.asad120@gmail.com; Tel.: +966-504658305

Abstract

Drying shrinkage is a critical durability issue in concrete structures, particularly in high-strength concrete (HSC), which is more susceptible to early-age cracking due to its low water–cement ratio and dense microstructure. This study experimentally evaluates the restrained drying shrinkage behavior of fiber-reinforced concretes with compressive strengths ranging from 23 to 84 MPa, employing a total of 84 ASTM C1581 ring specimens exposed to three exposure conditions: outdoor climate, indoor laboratory conditions (25 °C, 50% RH), and a controlled chamber (50 °C, 30% RH). Plain concretes exhibited increasing shrinkage with both strength and environmental severity. Under indoor exposure, 90-day shrinkage reached approximately 660 $\times$ 10^{-6} (23 MPa), 291 $\times$ 10^{-6} (40 MPa), 753 $\times$ 10^{-6} (60 MPa), and 338 $\times$ 10^{-6} (84 MPa), with high-strength mixes showing greater cracking susceptibility. Fiber incorporation significantly mitigated both strain and cracking in a dosage-dependent manner. Steel fibers at 1.0–1.5% reduced shrinkage by up to 75% in 40–60 MPa concretes, while polypropylene fibers at 0.25–0.5% achieved reductions up to 66% and eliminated cracking in several cases. Results demonstrate that concrete strength, exposure condition, fiber type, and dosage collectively govern shrinkage and cracking resistance.

Keywords: drying shrinkage; fiber-reinforced concrete; high-strength concrete; durability performance; crack mitigation; and environmental exposure

1. Introduction

Drying shrinkage is a major time-dependent deformation in concrete, driven primarily by moisture loss from the pore system to the surrounding environment. Specifically, as water migrates toward exposed surfaces and evaporates, capillary tension and related physicochemical mechanisms cause a net volume reduction, which may range from 1325 to 2065 μm/m in certain lightweight concretes and increases of up to 94.8% in recycled aggregate concrete, often causing surface and internal cracking [1]. When this deformation is restrained by internal reinforcement, sub-base friction, or boundary conditions, tensile stresses build up and can lead to micro- and macro-cracking. These shrinkage-induced cracks compromise serviceability, accelerate the ingress of chlorides and other aggressive agents, and ultimately reduce durability and structural safety, especially in slabs, pavements, bridge decks, thin walls, and other elements with high surface-to-volume ratios [2–4]. The issue is particularly critical in modern high-strength concretes, which often contain higher cement contents, low water–binder ratios, and supplementary cementitious

Check for updates

Received: 11 March 2026
Revised: 13 April 2026
Accepted: 27 April 2026
Published: 13 May 2026

Copyright: © 2026 by the authors. Licensee MDPI, Basel, Switzerland. This article is an open access article distributed under the terms and conditions of the Creative Commons Attribution (CC BY) license.

materials. Such mixes tend to exhibit refined pore structures and more intense hydration, making them prone to higher autogenous and drying shrinkage strains compared with conventional normal-strength concrete [5–7].

Notably, in high-strength concrete with limited internal moisture, both autogenous and drying shrinkage contribute to elevated cracking potential, whereas drying shrinkage is generally the dominant mechanism in normal-strength concrete. These mechanisms differ fundamentally in their driving forces and environmental interactions. Autogenous shrinkage is driven by self-desiccation, where the chemical consumption of water during cement hydration reduces internal relative humidity within capillary pores, creating negative capillary pressure that leads to macroscopic contraction [8,9]. This mechanism is particularly dominant in high-performance concrete with low water-to-cement (w/c) ratios (typically <0.40), where insufficient water is available to fill the voids created by chemical shrinkage. Drying shrinkage, conversely, originates from moisture exchange with the environment. As water evaporates from capillary pores into the lower-humidity atmosphere, menisci form and create capillary tension analogous to autogenous shrinkage but originating from the surface inward. The loss of adsorbed water from calcium-silicate-hydrate gel as drying continues leads to additional contraction. Unlike autogenous shrinkage, drying shrinkage is the primary concern for normal-strength concrete with higher w/c ratios, where moisture loss to the exterior is the dominant factor.

The drying shrinkage induces tensile stresses, leading to cracking and the risk of durability-related problems [10] surface quality and serviceability [11], internal warping, external deflection, and micro- or macro-cracking, all of which compromise the long-term reliability and performance of concrete structures [12]. Among the available approaches, fiber reinforcement has emerged as a widely adopted and efficient solution. Numerous studies have demonstrated that incorporating an adequate volume of fibers can substantially reduce drying shrinkage-related cracking. Rather than eliminating shrinkage strain itself, fibers primarily act by bridging developing cracks, controlling their width and distribution, and improving the early mechanical properties of concrete [13]. Their presence promotes a more uniform distribution of internal tensile stresses, reduces stress concentrations, and enhances tensile and flexural strengths [4]. While cracks in plain concrete typically form randomly under combined compressive, shear, and tensile stresses, the inclusion of fibers alters crack propagation patterns. Cracks tend to align relative to fiber orientation, and fibers function as effective bridges across crack planes, facilitating load transfer, limiting shrinkage-induced deflections, and improving overall structural performance [14].

Building on this understanding of the mechanisms by which fibers control crack initiation and propagation, the use of discrete fiber reinforcement has become increasingly common as a practical strategy to mitigate shrinkage cracking while maintaining or enhancing mechanical performance in both normal- and high-strength concretes. Steel, polypropylene, glass, basalt, and other synthetic or natural fibers form a three-dimensional reinforcing network within the cementitious matrix that bridges microcracks, redistributes tensile stresses, and improves toughness and ductility [4,6,15,16]. Numerous experimental studies have demonstrated that appropriately selected fiber systems can significantly reduce the severity of drying shrinkage damage, not necessarily by eliminating shrinkage strain, but by transforming wide, localized cracks into finer and more uniformly distributed crack patterns with reduced widths [3]. For instance, polypropylene and glass fibers have been reported to decrease drying shrinkage and delay or narrow restrained shrinkage cracks in high-strength concretes, while basalt and steel fibers have shown improved shrinkage performance and enhanced fatigue resistance in pavement-type concretes [2]. Comprehensive reviews of steel-fiber-reinforced and high-performance fiber-reinforced concretes further emphasize that shrinkage behavior is governed by a complex interac-

tion among fiber type, volume fraction, geometry, and hybridization strategy, as well as curing practices and ambient environmental conditions [7,17]. Despite these advances, a systematic understanding of how fiber reinforcement modifies the drying shrinkage behavior of normal- versus high-strength concretes under different ambient environments remains limited. This gap motivates focused experimental research on the drying shrinkage behavior of fiber-reinforced normal- and high-strength concrete under varied ambient conditions, intending to clarify these interactions and provide more reliable guidance for design and durability assessment.

To address shrinkage-related cracking, fiber-reinforced concrete (FRC) has gained significant attention as an effective means of enhancing both durability and mechanical performance in modern infrastructure. Compared with plain concrete, FRC incorporates discrete natural or synthetic fibers within the cementitious matrix, forming a three-dimensional reinforcing network that improves tensile capacity, ductility, and crack control. Although drying shrinkage—driven by moisture loss—remains a primary cause of cracking, stiffness degradation, and durability loss, particularly in restrained structural elements and pavements [18,19]. The inclusion of fibers helps mitigate these effects by bridging microcracks and redistributing internal tensile stresses. This function is especially important in high-strength and high-performance concretes, which typically possess lower water–binder ratios and denser microstructures, making them more susceptible to autogenous and drying shrinkage as well as crack localization [7,20]. Various fiber types—including steel, polypropylene, glass, and carbon—have been employed to enhance crack resistance, energy absorption, and impact performance, thereby improving the long-term dimensional stability of concrete exposed to drying conditions [21–23]. Owing to these advantages, FRC is increasingly applied in industrial floors, storage facilities, pavements, and protective structures where resistance to cracking, impact loads, and environmental deterioration is essential [24].

In structural applications, steel fibers are frequently used in combination with conventional reinforcement to reduce cracking and enhance resistance to impact, fatigue, shrinkage, and thermal stresses [25]. Although high-strength concrete provides superior compressive strength and durability, its increased brittleness with higher strength levels makes it particularly vulnerable to shrinkage-induced cracking [26,27]. The incorporation of fibers—especially steel fibers—has been shown to significantly improve ductility, toughness, and residual load-bearing capacity by effectively bridging cracks and redistributing tensile stresses [28–30]. Experimental evidence further indicates that steel fiber contents of up to approximately 1% by volume can increase splitting tensile strength by as much as 79% and enhance residual strength, thereby providing an efficient means of mitigating shrinkage-related damage in both normal- and high-strength concretes [31].

The effectiveness of such fiber-based mitigation strategies becomes particularly important under severe environmental conditions. Drying shrinkage is a major concern in arid climates, such as those prevalent in Saudi Arabia, where a large disparity between the internal humidity of concrete and low ambient humidity accelerates moisture loss from capillary pores [27,32–34]. In high-strength concrete with limited internal moisture, both autogenous and drying shrinkage contribute to elevated cracking potential [35–37], whereas drying shrinkage is generally the dominant mechanism in normal-strength concrete [38]. Cracking typically occurs when tensile stresses induced by restrained shrinkage—arising from foundations, reinforcement, or adjacent structural elements—exceed the tensile strength of the concrete. Slender members with large, exposed surface areas are especially vulnerable, and as drying initiates at the surface, shrinkage cracks tend to form externally and propagate inward over time [36,39,40]. These observations highlight that environmental exposure plays

a decisive role in governing the onset and severity of shrinkage cracking, underscoring the need to evaluate fiber-reinforced concrete performance under realistic climatic conditions.

A substantial body of research has investigated shrinkage behavior in various fiber-reinforced concrete systems, particularly in high- and ultra-high-performance fiber-reinforced concretes (HPFRC/UHPFRC) [5,41]. These studies have examined both autogenous and drying shrinkage under diverse curing regimes, including ambient, sealed, steam, and heat curing, and have linked shrinkage development to hydration kinetics, pore structure refinement, and moisture transport mechanisms. Research has shown that fiber type, dosage, and geometry significantly influence crack control and time-dependent deformation, while environmental factors such as temperature, relative humidity, and exposure conditions strongly govern shrinkage evolution [7,20]. Additional investigations incorporating moisture transport measurements and numerical modeling have further highlighted the coupling between internal moisture loss and shrinkage strain. Across these studies, key influencing parameters consistently identified include concrete strength level and binder composition, fiber characteristics, curing regime, ambient exposure, and restraint conditions. However, much of the existing work focuses either on specialized concrete (e.g., UHPFRC, seawater sea-sand concrete, alkali-activated systems, pavement bases) or on a single concrete strength class, such as high-strength concrete [15] or self-consolidating concrete under limited environmental conditions.

Despite these advances, important gaps remain in the literature. Direct, systematic comparisons between fiber-reinforced normal-strength and high-strength concretes tested under identical and controlled ambient temperature–humidity regimes are scarce. Most studies evaluate either conventional or high-performance mixtures separately, often with different mix designs, exposure conditions, or testing protocols, limiting the ability to quantify how strength level interacts with fiber reinforcement and environmental exposure in governing drying shrinkage [7,20,41]. Standardized ring tests are typically performed under controlled laboratory conditions to assess cracking potential [42,43]. A significant novelty of this work is the direct comparison of performance across three distinct environments: natural outdoor climate, controlled indoor conditions (25 °C, 50% RH), and a severe-drying chamber (50 °C, 30% RH). This bridges the "reality gap" by demonstrating how laboratory-derived shrinkage trends translate to structures exposed to real-world climatic fluctuations. While literature has explored low-volume hybrid fiber strategies for bridge decks [44], this paper identifies the specific dosages (0.5–1.5% for steel and 0.1–0.5% for polypropylene) required to delay the age of first cracking across a broad range of concrete strength-to-exposure combinations. Furthermore, fiber effectiveness is frequently assessed under a single curing or environmental condition, leaving uncertainty regarding the robustness of shrinkage mitigation strategies across varying climates, particularly hot-dry environments. There is also a gap between free-shrinkage characterization and performance under realistic restraint conditions, and existing prediction models—largely calibrated for plain normal-strength concrete—often fail to accurately capture early-age and strength-dependent shrinkage behavior of fiber-reinforced systems.

The novelty of this research also lies in its systematic approach to bridge the gap between standardized laboratory testing and field performance. While standard ASTM C1581 [45] protocols are essential for assessing cracking capacity, they often lack validation under variable environmental conditions. In addition, the experimental results will enable benchmarking of observed shrinkage behavior against existing prediction models, which have predominantly been calibrated for plain or single-strength concretes and often neglect the influence of fiber reinforcement.

Accordingly, the objective of this study is to experimentally investigate the drying shrinkage behavior of fiber-reinforced normal-strength and high-strength concrete un-

der different ambient temperature and relative humidity conditions, to clarify strength-environment-fiber interactions, quantifying fiber efficiency across strength classes, and generating reliable data for improved shrinkage prediction and durability-oriented design. The research aims to: (1) evaluate the influence of fiber type (steel and polypropylene) and volume fraction on shrinkage strain, crack initiation, and crack propagation across concrete strength classes (23, 40, 60, and 84 MPa) under both free and restrained conditions; (2) elucidate the interactive effects among concrete strength level, environmental exposure, and fiber type and dosage on drying shrinkage development, internal moisture evolution, and cracking propensity; (3) improve the mechanistic understanding of fiber-reinforced systems by examining the evolution of drying shrinkage in relation to internal moisture variation; and (4) generate a comprehensive experimental database of restrained ring test results under controlled ambient conditions to serve as a foundation for benchmarking and validation of existing shrinkage prediction models in subsequent research phases.

2. Experimental Materials and Procedure

2.1. Materials

2.1.1. Cementitious Materials

Portland cement Type II, complying with ASTM C150 requirements [46], was used in all concrete mixtures for this study. The chemical characteristics of this cement are presented in Table 1.

Table 1. Properties of Portland Cement.

Oxides	CaO	SiO_2	Al_2O_3	Fe_2O_3	MgO	K_2O	SO_3
Weight (%)	62.85	22.3	3.38	5.56	3.55	0.64	1.71

2.1.2. Fibers

Polypropylene and steel fibers were used in this study to comparatively evaluate the efficiency of adding both polymeric and metallic fibers into concrete. The selection of polypropylene and steel fibers was based on their complementary roles in managing shrinkage at different scales (micro vs. macro) and stages (early-age vs. long-term), which is critical for the wide range of concrete strengths (23–84 MPa) investigated in this study. Polypropylene fibers were selected with a high aspect ratio of 559 and an extremely fine diameter of 0.034 mm. These specifications were chosen to maximize the number of fibers per unit volume, creating a dense three-dimensional reinforcing network [4]. This high fiber count is specifically targeted at controlling early-age micro-cracking. Because of their small diameter and high aspect ratio, these fibers are highly effective at intercepting and bridging micro-cracks before they coalesce into macro-cracks [2,13]. This theoretical basis is confirmed by our results, where PP fibers at very low dosages (0.25–0.5%) achieved shrinkage reductions exceeding 60% and eliminated visible cracking in several strength classes, particularly under outdoor exposure.

Steel fibers (60 mm length, 0.8 mm diameter, aspect ratio 75) were selected based on evidence that steel fiber reinforcement can increase splitting tensile strength by up to 79% and provide significant development length and mechanical anchorage across macro-crack planes [16]. The longer fiber length and lower aspect ratio provide sufficient stiffness and tensile strength (>1000 MPa modulus of 200 GPa) for resisting the substantial tensile stresses generated as drying progresses, especially in high-strength concrete, where shrinkage-induced stresses are more intense [30,41]. The complementary selection of these polymeric and metallic fiber systems enables systematic evaluation of how fiber type, volume fraction, and geometry interact to control crack width and distribution, transforming localized

cracks into finer patterns with reduced widths—the primary mechanism by which fibers mitigate shrinkage-related damage in both normal- and high-strength concretes. The fiber selection also accounted for the concrete strength level. While PP fibers provided an efficient early-stage defense through micro-crack bridging [14], the steel fibers acted as long-term reinforcement, redistributing internal tensile stresses to prevent localized failure. Table 2 shows a summary of the physical parameters of these fibers.

Table 2. Physical characteristics of used fibers in the experiment.

Fiber Type	Length (mm)	D (mm)	AR (L/d)	Density (kg/cm^3)	TS (MPa)	ME (GPa)	MP (°C)
Polypropylene fibers	19	0.034	559	910	>400	3.5–4.5	~160
steel fiber	60	0.8	75	7850	>1000	200	>1400

D: Diameter, AR: Aspect Ratio, TS: Tensile Strength, ME: Modulus of Elasticity, MP: Melting point.

2.1.3. Aggregates Grading and Material Properties

Aggregate grading plays a vital role in ensuring the workability, strength, and overall performance of concrete mixtures. The suitability of aggregate grading depends on various factors, such as the maximum aggregate size, cement content, mixture type, and intended application. Aggregate selection followed ASTM C33 and C16 specifications [47,48], while cement properties complied with ASTM C150 [49]. The proportioning strategy followed standard industry practices by systematically varying cement content and water-to-cement ratio to achieve the target strength range of 23–84 MPa. Silica fume was incorporated only in the high-strength concrete mix (84 MPa) as a supplementary cementitious material. In this study, natural sand with a fineness modulus of 2.95 was used as the fine aggregate, while the coarse aggregate consisted of crushed stone with a maximum nominal size of 9.5 mm. Both aggregates were sourced from a local company. Sieve analysis of the coarse and fine aggregates is illustrated in Figure 1.

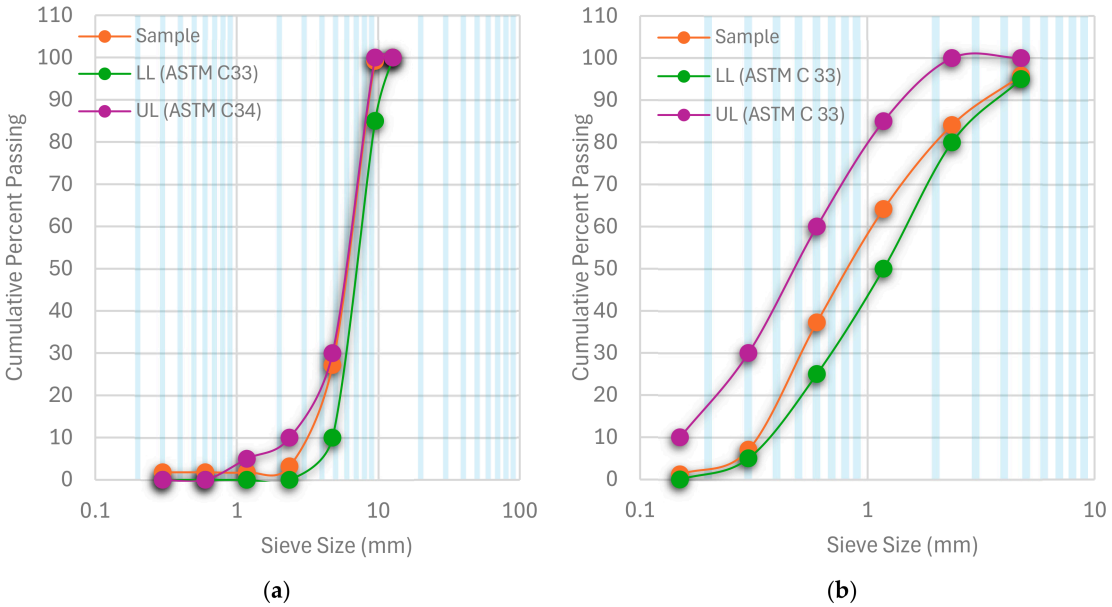


Figure 1. Sieve Analysis of the aggregates: (**a**) Coarse Aggregate and (**b**) Wash Sand.

2.2. Mixing Compositions and Specimen Preparation

The mix designs in this study were engineered to span a broad compressive strength range from 23 MPa to 84 MPa by systematically reducing the water-to-binder (w/c) ratio and optimizing the cementitious matrix [50]. For the 84 MPa high-strength concrete mixes,

a low ratio (e.g., 0.25) was maintained, supported by a high binder content (500–550 kg/m^3) to ensure a dense microstructure [51]. The aggregate dosage was determined based on the principle of maximum packing density to create a rigid internal skeleton [52]. The 23 MPa reference mix employs conventional proportioning with a w/c of 0.70 and no admixtures. As target strength increases, the w/c ratio decreases progressively (0.40, 0.33, 0.25), necessitating adjustments to aggregate quantities to maintain workability. The 84 MPa mix includes silica fume at 10% by cement mass, which is essential at this ultra-high strength level to refine the pore structure, fill the microscopic voids between cement particles and the aggregate-paste interface, and enhance hydration products to form additional calcium-silicate-hydrate $(C-S-H)$ gel [51,52], and achieve the required compressive strength [53] when combined with the extremely low w/c ratio of 0.25 [51]. This graduated approach allows systematic evaluation of how concrete strength interacts with fiber reinforcement and environmental exposure in governing drying shrinkage behavior.

A total of 84 ring specimens, including nine ring specimens of plain concrete without fiber dosage and 15 fiber-reinforced specimens at each strength level, were cast following the ASTM C1581 standard protocol, comprising four concrete strength levels (23, 40, 60, and 84 MPa) using materials specified in Table 3, with varying fiber contents ranging from 0 to 1.5% by volume. The concrete mixes were prepared and externally vibrated using a shaking table to ensure proper compaction, then formed in a circular ring mold configuration following existing studies [54–56] as illustrated in Figure 2. The summary of the 84 ASTM C1581 ring specimens' distribution is given in Table 4. This procedure is suitable for evaluating restrained drying shrinkage. After casting, the upper surfaces of the rings were sealed with a silicone-based material to restrict evaporation to only the outer circumferential surface, deliberately creating a one-directional drying path from the exposed outer circumference toward the inner radius. This simulates realistic concrete behavior where external surfaces dry first while internal portions remain comparatively wetter. For the thin-wall ring geometry employed in this study (37.5 mm wall thickness), the resulting moisture gradient across the radial cross-section is relatively steep, with self-restraint effects less pronounced compared to thicker specimens. The outer PVC molds were removed 24 h after casting. Following demolding, three electrical strain gauges were affixed to the outer surface of each ring at equal angular spacing to monitor shrinkage strain development over time. This multi-point measurement approach captures any non-uniform strain development resulting from non-uniform moisture loss. By maintaining identical boundary conditions across all specimens, the comparative influence of fiber reinforcement and concrete strength on shrinkage behavior remains valid, with any observed variations in cracking age and shrinkage strain attributable to material composition and environmental exposure conditions rather than inconsistencies in moisture loss.

Table 3. Mix composition of concrete.

Mix No.	Strength (MPa)	w/c	Admixture (% of Cement)	Silica Fume (%)	FA (kg/m^3)	CA (kg/m^3)
1	23	0.70	0.0	0.0	525	1050
2	40	0.40	1.0	0.0	770	560
3	60	0.33	5.0	0.0	770	560
4	84	0.25	5.0	10.0	350	700

FA: Fine Aggregate, CA: Coarse Aggregate.

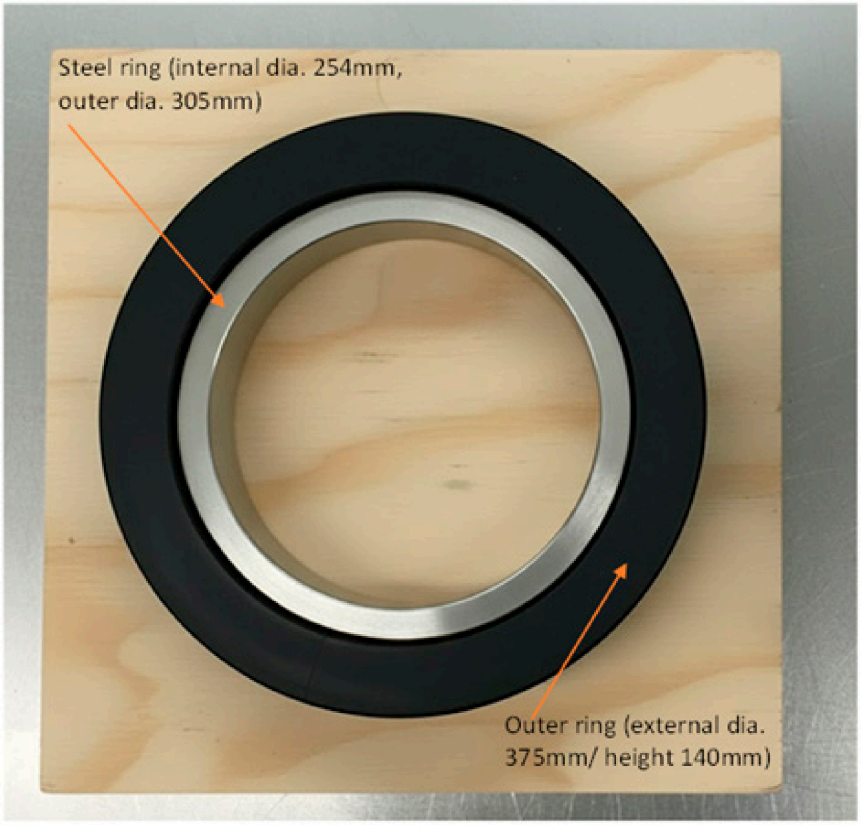


Figure 2. Dimension of the ring specimen.

Table 4. Summary Distribution of 84 ASTM C1581 Ring Specimens.

Concrete Strength (MPa)	Plain Concrete (0% Fiber)	Fiber-Reinforced Concrete (0.25–1.5% Fiber)
23	9	15
40	9	15
60	9	15
84	9	15
Total	36	60

2.3. Testing Procedure

The specimens' drying shrinkage and cracking behavior were studied under three environmental exposure conditions, as shown in Table 5: outdoor exposure (O), indoor laboratory conditions (I), and a controlled environmental chamber (C). Outdoor specimens were subjected to naturally fluctuating temperature and humidity. Indoor specimens were placed in a controlled laboratory environment at 25 °C temperature and 50% relative humidity. Specimens in the environmental chamber were tested under constant conditions of 50 °C and 30% relative humidity. Visual inspections were carried out twice daily for outdoor and indoor specimens to record the appearance, timing, and extent of cracking. A special microscope setup was used to measure the crack width at each crack location, taking three readings (top, center, bottom) and averaging them. The specimens in the controlled chamber were monitored without disturbance during the testing period, and final crack assessments were performed at the end.

Table 5. Exposure conditions employed in the Study.

Condition	Temperature and Humidity	Description
Outdoor (O)	Fluctuating natural climate	Exposed to sunlight, wind, and daily changes in temperature and humidity.
Indoor (I)	25 °C, 50% RH	Stable laboratory environment under controlled moderate conditions.
Controlled (C)	50 °C, 30% RH	Constant high-temperature, low-humidity chamber for severe drying simulation.

Specimens in the controlled chamber underwent visual crack assessment exclusively at the end of the test period rather than at intermediate intervals. This methodological choice was deliberate and necessary: opening the chamber for frequent inspections would have disrupted the precise, constant environmental parameters (50 °C, 30% RH) that define the controlled drying simulation. Such disturbances would introduce uncontrolled variability in relative humidity and temperature exposure, thereby invalidating the severity basis for chamber testing. This trade-off prioritizes environmental control integrity over crack initiation timing data. The final crack area measurements nonetheless provide a cumulative assessment of each fiber type and dosage's restraint capability under sustained severe drying, enabling meaningful comparative analysis of fiber effectiveness across concrete strengths and exposures. Each specimen was systematically labeled to reflect its fiber type, concrete strength, environmental condition, and fiber volume fraction (e.g., PF-40-C-0.25).

2.3.1. Moisture Loss Uniformity

Following demolding, three electrical strain gauges were affixed to the outer surface of each ring at equal angular spacing to monitor shrinkage strain development over time. This multi-point measurement approach captures any non-uniform strain development resulting from non-uniform moisture loss. The intentional sealing of the upper specimen surface creates a one-directional drying path from the exposed outer circumference toward the inner radius. To assess the uniformity of moisture-induced shrinkage under this condition, strain data from all three electrical strain gauges were analyzed across all exposure conditions and concrete strengths. The three-gauge measurement system allowed for a rigorous assessment of shrinkage uniformity. At outdoor exposure, restrained drying shrinkage strains were measured at curing ages of 14, 28, 56, and 90 days for all concrete strengths (23 MPa, 40 MPa, 60 MPa, and 84 MPa). The strain ranges, typically within 10–15% of the mean value, demonstrate that despite the unidirectional evaporation restriction to the outer circumferential surface, the radial moisture gradient developed relatively uniformly throughout the specimen.

The baseline plain concrete shrinkage strains, at controlled chamber exposure (50 °C and 30% RH), reached 757 $\times$ 10^{-6} (23 MPa), 567 $\times$ 10^{-6} (40 MPa), 704 $\times$ 10^{-6} (60 MPa), and 688 $\times$ 10^{-6} (84 MPa) in 90 days. Measurements from the three gauges at equal angular spacing showed consistent development patterns, validating the assumption of relatively uniform radial moisture loss despite the one-directional evaporation restriction. All concrete exhibited pronounced time-dependent restrained drying shrinkage at indoor exposure (25 °C and 50% RH). Control specimens exhibited shrinkage at 90 days of 659.5 $\times$ 10^{-6} (23 MPa), 290.6 $\times$ 10^{-6} (40 MPa), 752.8 $\times$ 10^{-6} (60 MPa), and 338.3 $\times$ 10^{-6} (84 MPa). The 60 MPa concrete exhibited the highest absolute shrinkage, increasing by approximately 378 $\times$ 10^{-6} ($\approx$101%) from 14 to 90 days.

2.3.2. Data Quality and Measurement Verification

To ensure data reliability and verify measurement consistency, three electrical strain gauges were affixed to the outer surface of each ring at equal angular (120°) spacing to monitor shrinkage strain development over time. Data repeatability was verified by comparing these three independent measurements; variations remained within 10–15% of the mean, confirming uniform radial shrinkage. These results confirm that despite the unidirectional evaporation restriction to the outer circumferential surface, the radial moisture gradient developed relatively uniformly throughout the specimen. All 84 specimens were prepared and tested under identical boundary conditions following the ASTM C1581 standard protocol, ensuring that any observed variations in cracking age and shrinkage strain are attributable to material composition and environmental exposure conditions rather than procedural inconsistencies. By maintaining identical boundary conditions across all specimens, the comparative influence of fiber reinforcement and concrete strength on shrinkage behavior remains valid and reliable. Furthermore, the observed trends—such as the dosage-dependent effectiveness of steel fibers, the high efficiency of polypropylene fibers at low dosages, and the strength-dependent shrinkage susceptibility—were consistent across all three exposure conditions. This cross-validation across different environmental scenarios provides additional confidence in the reliability of the findings.

3. Result and Discussion

3.1. Strain Measurements of Drying Shrinkage

The consistent strain measurements across the three gauges at equal circumferential spacing confirm that the specimen preparation methodology does not introduce significant non-uniformity in shrinkage strain development. By maintaining identical boundary conditions across all 84 specimens, any observed variations in cracking age and shrinkage strain are attributable to material composition and environmental exposure conditions rather than inconsistencies in moisture loss, validating the comparative influence of fiber reinforcement and concrete strength on shrinkage behavior. Fibers demonstrated significant strain-reduction effectiveness across all exposure conditions. Steel fibers at outdoor exposure showed effectiveness increasing with fiber dosage, with 0.5% SF reducing shrinkage at 90 days by approximately 2% (23 MPa), 45% (40 MPa), 38% (60 MPa), and 23% (84 MPa) relative to control specimens. Polypropylene fibers were particularly effective at low dosages, with 0.1% PF achieving shrinkage reductions at 90 days ranging from approximately 35–47% for 23–60 MPa concretes.

3.1.1. Drying Shrinkage Strains at Outdoor Exposure

Concrete specimens exposed to natural outdoor conditions exhibited distinct drying shrinkage behaviors based on their compressive strength and fiber content. Figure 3 illustrates the strain gauge measurements for outdoor concrete ring specimens prepared with concrete having 28-day compressive strengths of 23 MPa, 40 MPa, 60 MPa, and 84 MPa. In these plots, the thinner lines denoted as (C) represent the plain concrete control specimens (0% fiber), which serve as the critical baseline for evaluating the mitigation efficiency of steel and polypropylene fibers. Measurements were illustrated in these figures at curing ages of 14, 28, 56, and 90 days to evaluate the restrained shrinkage behavior under natural environmental exposure. As shown across subfigures (a–d), the control specimens consistently exhibited the steepest strain development curves, with the 60 MPa and 84 MPa mixes reaching peak 90-day strains of 575 and 520 $\times 10^{-6}$, respectively. This higher susceptibility in high-strength matrices is primarily attributed to the synergistic effect of intense internal self-desiccation (autogenous shrinkage), and drying shrinkage, a phenomenon driven by the dense microstructure and low water-to-binder ratios character-

istic of high-performance concrete [5,15]. Conversely, the 23 MPa control mix displayed a more gradual strain increase to 476 × 10^{-6}, as its more porous matrix allows for slower development of internal capillary tension.

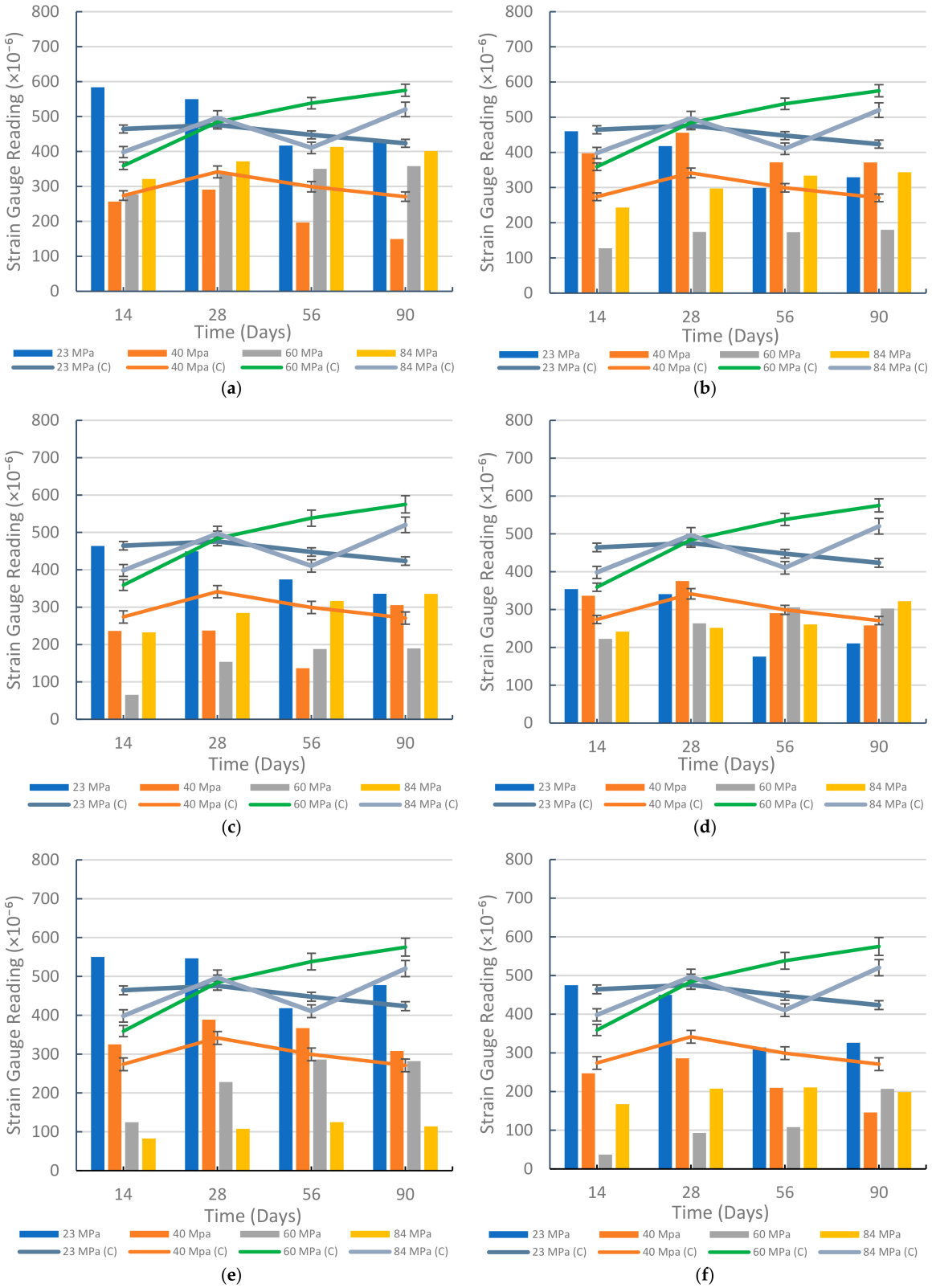


Figure 3. Strain gauge measurements for outdoor ring specimens made with concrete of 28-day compressive strengths: (**a**) 0.5% SF, (**b**) 1.0% SF, (**c**) 1.5% SF (**d**) 0.1% PF, (**e**) 0.25% PF and (**f**) 0.5% PF.

The introduction of fibers effectively "flattened" these strain development curves by bridging micro-cracks and redistributing internal stresses throughout the matrix. Steel fibers (SF) addition significantly mitigates restrained drying shrinkage strain through a clear dosage-dependent mechanism, with effectiveness peaking at the 1.5% volume fraction. As illustrated in the outdoor exposure results, steel fibers function as a macro-scale reinforcement that bridges developing crack planes, utilizing their high elastic modulus (200 GPa) and tensile strength (>1000 MPa) to resist the substantial internal tensile stresses generated by moisture loss [15,16]. Detailed analysis of the 90-day data shows that while a low dosage of 0.5% SF provides moderate reductions—ranging from 23% in 84 MPa concrete to 45% in 40 MPa concrete—increasing the dosage to 1.5% SF achieves superior mitigation. Specifically, for the 60 MPa strength class, 1.5% SF reduced the shrinkage strain from 575 $\times$ 10^{-6} to 190 $\times$ 10^{-6}, representing a 67% reduction compared to the plain concrete control (C). However, the mitigation was less pronounced in the ultra-high-strength 84 MPa mix, where the same 1.5% dosage yielded only a 35% reduction (from 520 to 336 $\times$ 10^{-6}, likely due to the higher autogenous shrinkage component and denser matrix, which increases the intensity of internal stress concentrations [17,37].

As shown in Figure 3d–f, the addition of polypropylene fibers leads to a significant reduction in restrained drying shrinkage strain compared to the plain concrete control specimens. Across the various concrete strength levels depicted in the subfigures, the fiber-reinforced mixes consistently maintain a lower strain profile than the baseline control specimens. Research into these fiber-matrix interactions has demonstrated that even a low fiber volume fraction of 0.1% can result in a 35–47% decrease for 23–60 MPa concretes in the ultimate dry shrinkage strain observed at 90 days. Increasing PF content to 0.25% and 0.5% further reduced shrinkage, with 60 MPa concrete reaching values as low as 94–108 $\times$ 10^{-6} at early ages and remaining below 210 $\times$ 10^{-6} at 90 days—representing reductions exceeding 60% compared with control. By incorporating these fibers, the development of strain is significantly attenuated, leading to enhanced long-term dimensional stability and a more gradual development of internal stresses relative to the unreinforced control specimen [57,58]. The significant impact of polypropylene fibers on the strain development is attributed to several integrated microstructural and mechanical mechanisms. One primary reason is the improvement of the internal pore structure; the fibers connect capillary pores at the micron and lower levels, which reduces the internal capillary stress that acts as the primary driving force for the shrinkage process. Furthermore, the fibers form a complex three-dimensional system within the matrix and create a water film on their surfaces, both of which help to limit the migration and loss of water during the drying period Mechanically, the high surface-area-to-volume ratio of the fibers allows for effective interlocking with the surrounding cement paste, facilitating a more diffuse build-up of internal stresses and effectively restraining micro-level movements within the matrix [58,59]. These combined effects ensure that the overall magnitude of shrinkage is managed more effectively than in the plain concrete baseline, resulting in the "flattened" strain trajectories observed in the experimental results [58,60].

3.1.2. Drying Shrinkage Strains at Controlled Chamber

Strain gauge measurements for restrained ring specimens tested under controlled environmental conditions (50 °C temperature and 30% relative humidity) across four concrete compressive strength levels: 23 MPa, 40 MPa, 60 MPa, and 84 MPa are presented in Figure 4. This controlled exposure environment was specifically designed to accelerate moisture loss while maintaining constant temperature and humidity, thereby eliminating the confounding variables inherent in outdoor and indoor exposure conditions. The plain concrete control specimens (0% fiber) in Figure 4 establish the critical

baseline for evaluating fiber-reinforcement efficacy. At 90 days under controlled exposure, the baseline shrinkage strains increased with time, reaching final values of 757 $\times$ 10^{-6} (23 MPa), 567 $\times$ 10^{-6} (40 MPa), 704 $\times$ 10^{-6} (60 MPa), and 688 $\times$ 10^{-6} (84 MPa) microstrains. The development from 14 to 90 days demonstrates substantial time-dependent behavior, with the 23 MPa mix exhibiting a modest 5% increase (718 to 757 $\times$ 10^{-6}), while the higher-strength concretes—particularly the 60 MPa and 84 MPa mixes—showed more pronounced increases of 34% (527 $\rightarrow$ 704 $\times$ 10^{-6}) and 44%, respectively. This strength-dependent acceleration in late-stage shrinkage reflects the intensified internal capillary tension and differential moisture gradients characteristic of dense, low water-to-cement ratio matrices.

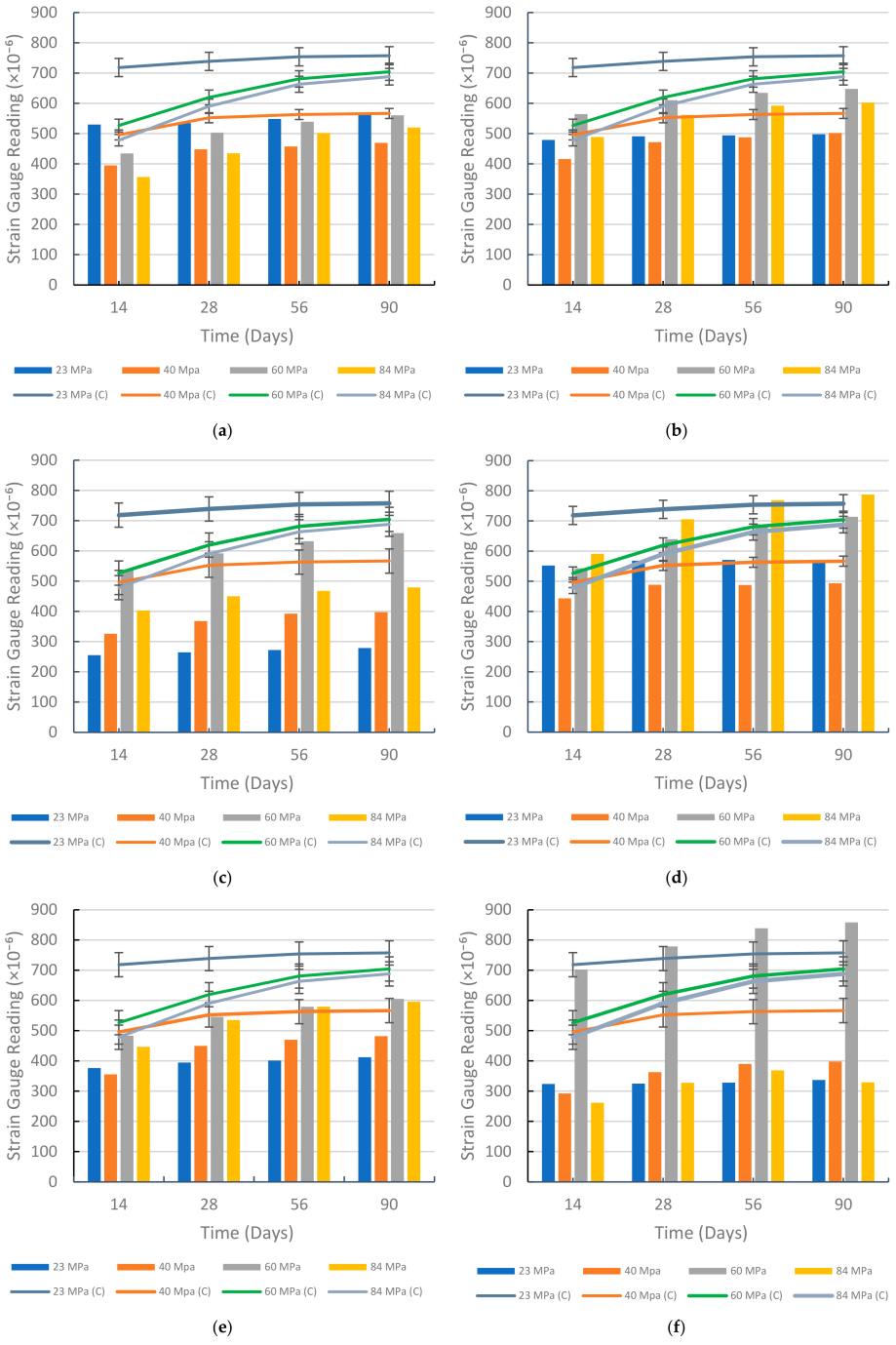


Figure 4. Strain gauge measurements for controlled ring specimens made with concrete of 28-day compressive strengths: (**a**) 0.5% SF, (**b**) 1.0% SF, (**c**) 1.5% SF (**d**) 0.1% PF, (**e**) 0.25% PF and (**f**) 0.5% PF.

Relative to this controlled-exposure baseline at 90 days, Steel fiber addition produced consistent and dose-dependent shrinkage reduction across all strength levels. At the 0.5% dosage, strain gauge measurements reduced to 568, 469, 561, 520 $\times$ 10^{-6} microstrains for the 23/40/60/84 MPa concretes, corresponding to reductions of 25%, 17%, 20%, and 24%, respectively. Increasing the dosage to 1.0% steel fibers yielded more substantial improvements, with strain measurements of 498, 502, 648, and 602 $\times$ 10^{-6} microstrains (reductions of 34%, 11%, 8%, and 12%). The highest steel fiber dosage of 1.5% produced the most effective mitigation for low-strength concrete, reducing shrinkage to 279 $\times$ 10^{-6} microstrains at 23 MPa (63% reduction), though improvement at 60 MPa remained limited at only 6% reduction. Polypropylene fibers demonstrated more complex dosage and strength-dependent behavior under controlled exposure. At the 0.25% dosage, strains decreased to 412, 482, 605, and 596 $\times$ 329 $\times$ 10^{-6} microstrains, achieving reductions of 46%, 15%, 14%, and 13% for the respective strength levels. However, a counterintuitive finding emerged at the 60 MPa strength level with 0.5% polypropylene fibers: shrinkage increased to 858 $\times$ 10^{-6} microstrains (+22% relative to baseline 704 $\times$ 10^{-6}), while the same dosage proved highly effective at 23 MPa and 84 MPa, achieving 56% and 52% reductions, respectively.

This counterintuitive result—where 0.5% polypropylene fibers increased shrinkage by 22% (858 $\times$ 10^{-6} microstrains) at 60 MPa compared to the baseline 704 $\times$ 10^{-6}—reflects a strength-dependent optimization limitation rather than an inherent deficiency of the polypropylene fiber system. The phenomenon can be attributed to three interacting factors: First, at 60 MPa, the concrete matrix achieves intermediate densification and reduced porosity that impairs optimal fiber distribution and interfacial bonding, preventing the fiber network from achieving sufficient stress-bridging capacity. Second, the severe controlled drying environment (50 °C, 30% RH) intensifies moisture gradients and drying-induced stresses in this intermediate-strength matrix, which exceeds the restraining capacity of the selected 0.5% PF dosage. Third, the fiber effectiveness across the tested strength range (23, 40, 60, and 84 MPa) demonstrates a non-linear, strength-dependent relationship: while 0.5% PF achieved significant reductions at 23 MPa (56% reduction) and 84 MPa (52% reduction), the intermediate 60 MPa strength level represents a critical transition zone where the selected dosage could not effectively control shrinkage development. This finding indicates that optimal fiber dosages must be tailored to specific concrete strength and environmental exposure conditions rather than applied universally.

Bringing these performance comparisons together, the efficacy analysis reveals that steel fibers demonstrated superior and highly consistent shrinkage mitigation across all concrete strength levels under controlled exposure conditions. At equivalent dosages, steel fibers achieved predictable, dosage-dependent reductions ranging from 17% to 25% at 0.5% dosage and up to 63% at 1.5% dosage for lower-strength concrete, whereas polypropylene fibers exhibited strength-sensitive behavior that produced counterproductive outcomes at intermediate matrix densities. The superior performance of steel fibers at 60 MPa can be attributed to their higher elastic modulus and superior interfacial bonding capacity, which maintained effective stress-bridging even within denser, low-porosity matrices where polypropylene fiber distribution was impaired. In contrast, polypropylene fibers require careful dosage optimization relative to specific concrete strength classes, as the 0.5% dosage proved insufficient to restrain moisture-induced stresses within the intermediate 60 MPa matrix under severe drying conditions, resulting in a 22% shrinkage increase rather than reduction. From a practical design perspective, steel fibers are recommended for applications requiring reliable shrinkage control across varying concrete strength classes, while polypropylene fiber dosages must be calibrated specifically to matrix density and environmental severity to avoid counterproductive outcomes. It should be noted that these

findings are based on a single controlled exposure condition (50 °C, 30% RH), and fiber effectiveness may vary under field conditions involving cyclic temperature and humidity fluctuations, requiring further investigation across broader environmental exposure scenarios. Future studies should examine hybrid fiber combinations and intermediate dosage increments at the 60 MPa strength level to identify optimal reinforcement strategies for intermediate-strength concrete matrices.

3.1.3. Drying Shrinkage Strains at Indoor Exposure

Figure 5 presents strain gauge measurements from ring specimens subjected to indoor exposure conditions (25 °C and 50% relative humidity), providing a systematic assessment of restrained drying shrinkage behavior across four concrete strength classes: 23 MPa, 40 MPa,60 MPa, and 84 MPa. This controlled laboratory environment enables direct comparison of how concrete strength, fiber type, and fiber dosage influence shrinkage development over the testing period. The plain concrete control specimens (without fiber reinforcement) demonstrated pronounced time-dependent shrinkage development throughout the 90-day testing period. At 14 days, shrinkage strains for the control mixes ranged between 362 and 375 $\times$ 10^{-6} for both the 23 MPa and 60 MPa concretes, with the 40 MPa and 84 MPa specimens exhibiting intermediate values. By 90 days, the control specimens exhibited significantly elevated shrinkage, increasing to 659.5 $\times$ 10^{-6} (23 MPa), 290.6 $\times$ 10^{-6} (40 MPa), 752.8 $\times$ 10^{-6} (60 MPa), and 338.3 $\times$ 10^{-6} (84 MPa). A critical observation is that the 60 MPa concrete exhibited the highest absolute shrinkage value, increasing by approximately 378 $\times$ 10^{-6} (≈101%) from 14 to 90 days, while the 23 MPa, 40 MPa, and 84 MPa concretes increased by approximately 82%, 104%, and 115%, respectively. 3 This indicates that under constant indoor drying conditions, higher-strength concretes experience greater sustained shrinkage development despite their lower initial moisture content, contrary to expectations that higher-strength matrices would inherently resist moisture loss more effectively.

Steel fiber reinforcement demonstrated clear and consistent dose-dependent shrinkage mitigation across all concrete strength levels. At the lowest steel fiber dosage of 0.5%, shrinkage reduction at 90 days was approximately 10% (23 MPa), 32% (40 MPa), 40% (60 MPa), and 20% (84 MPa) relative to control specimens. Increasing the steel fiber content to 1.0% resulted in substantially stronger reductions, particularly for higher-strength concrete, with shrinkage decreasing to 195.7 $\times$ 10^{-6} for 60 MPa concrete (≈74% reduction). The highest steel fiber dosage of 1.5% provided the most effective mitigation, lowering 90-day shrinkage to 150 $\times$ 10^{-6} (40 MPa) and 163 $\times$ 10^{-6} (60 MPa), corresponding to reductions exceeding 75% compared with control specimens. 4 This superior performance is attributable to the high modulus of elasticity (200 GPa) and tensile strength (>1000 MPa) of steel fibers, enabling them to effectively resist the substantial internal tensile stresses generated by moisture loss.

Polypropylene fiber reinforcement also reduced shrinkage but exhibited markedly different behavior compared to steel fibers, demonstrating greater sensitivity to both dosage and concrete strength. At 90 days, the lowest polypropylene fiber dosage of 0.1% provided limited shrinkage control, whereas 0.25% polypropylene fiber reduced shrinkage by approximately 36% (23 MPa) and 41% (60 MPa). The highest polypropylene fiber dosage of 0.5% was particularly effective for intermediate-strength concretes, reducing shrinkage to 152 $\times$ 10^{-6} for 40 MPa (≈48% reduction) and 257 $\times$ 10^{-6} for 60 MPa (≈66% reduction). However, polypropylene fiber effectiveness demonstrated a non-linear, strength-dependent relationship across the tested strength range (23, 40, 60, and 84 MPa), with the intermediate 60 MPa strength level representing a critical transition zone where fiber dosage optimization becomes particularly important.

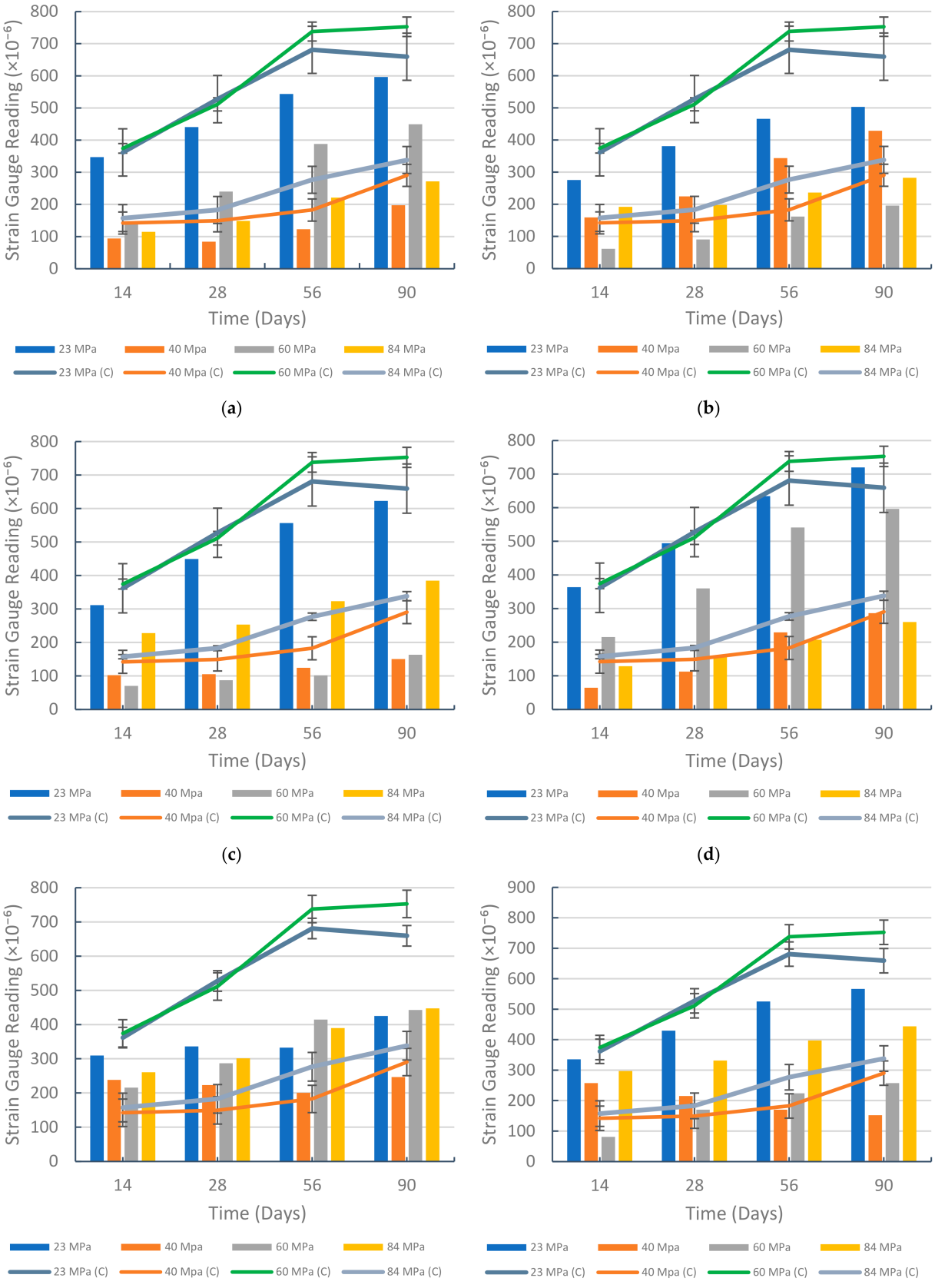


Figure 5. Strain gauge measurements for indoor ring specimens made with concrete 28-day compressive strengths: (**a**) 0.5% SF, (**b**) 1.0% SF, (**c**) 1.5% SF, (**d**) 0.1% PF, (**e**) 0.25% PF, and (**f**) 0.5% PF.

Overall, Figure 5 data demonstrate that steel fibers at dosages $\geq$ 1.0% provide the most robust shrinkage control under indoor drying conditions, while polypropylene fibers can achieve comparable reductions at higher dosages, especially for 40–60 MPa strength concretes. This finding underscores that under constant laboratory drying conditions with stable temperature and relative humidity, fiber type selection and dosage optimization cannot rely on single-parameter approaches but must account for the complex interplay between concrete strength, environmental severity, and fiber material properties. The data presented in Figure 5 establishes that fiber-reinforced concrete substantially outperforms plain concrete in controlling moisture-induced shrinkage under indoor exposure, with the magnitude of improvement varying systematically with strength class and fiber dosage, providing critical guidance for practical applications requiring controlled shrinkage performance.

3.1.4. Comparative Analysis of Shrinkage Development Rates

The comparative analysis of shrinkage kinetics reveals that environmental severity significantly influences the rate of development, though the magnitude of this impact is highly dependent on concrete strength. Restrained drying shrinkage strains exhibited markedly different development rates across the three environmental conditions tested, with indoor exposure demonstrating the most severe kinetics. Control specimens under outdoor exposure reached shrinkage strains of 423–476 $\times$ 10^{-6} $\mu\epsilon$ (23 MPa), 271–342 $\times$ 10^{-6} $\mu\epsilon$ (40 MPa), 359–575 $\times$ 10^{-6} $\mu\epsilon$ (60 MPa), and 398–520 $\times$ 10^{-6} $\mu\epsilon$ (84 MPa) between 14 and 90 days, yielding average development rates of approximately 0.36–1.42 $\mu\epsilon$/day. In contrast, controlled chamber exposure (50 °C, 30% RH) produced substantially higher baseline shrinkage strains, reaching 757 $\times$ 10^{-6} $\mu\epsilon$ (23 MPa), 567 $\times$ 10^{-6} $\mu\epsilon$ (40 MPa), 704 $\times$ 10^{-6} $\mu\epsilon$ (60 MPa), and 688 $\times$ 10^{-6} $\mu\epsilon$ (84 MPa) at 90 days. 2 From 14 to 90 days, the chamber condition showed only modest increase for 23 MPa (+5%), but much larger increases for higher strengths, particularly 60 MPa (527–704 $\times$ 10^{-6} $\mu\epsilon$, +34%) and 84 MPa (478–688 $\times$ 10^{-6} $\mu\epsilon$, +44%), indicating 1.1–3.5$\times$ faster development rates in denser mixes compared to outdoor conditions.

Under indoor exposure (25 °C, 50% RH), all concrete exhibited pronounced time-dependent restrained drying shrinkage with significantly higher growth rates than those observed at early ages. For control (plain) mixes, shrinkage at 14 days ranged between 362 and 375 $\times$ 10^{-6} $\mu\epsilon$ for 23 and 60 MPa concretes and increased steadily to 659.5 $\times$ 10^{-6} $\mu\epsilon$ (23 MPa), 290.6 $\times$ 10^{-6} $\mu\epsilon$ (40 MPa), 752.8 $\times$ 10^{-6} $\mu\epsilon$ (60 MPa), and 338.3 $\times$ 10^{-6} $\mu\epsilon$ (84 MPa) at 90 days. 4 The 60 MPa concrete exhibited the highest absolute shrinkage, increasing by approximately +378 $\times$ 10^{-6} $\mu\epsilon$ ($\approx$101%) from 14 to 90 days, while the 23 MPa, 40 MPa, and 84 MPa concretes increased by about 82%, 104%, and115%, respectively, yielding development rates of 3.87–4.97 $\mu\epsilon$/day and demonstrating 3.5–10.7$\times$ faster development compared to outdoor conditions. The interaction between concrete strength and environmental exposure significantly influenced shrinkage development patterns. Under outdoor conditions, lower-strength concretes (23–40 MPa) exhibited slower absolute development rates (0.36–0.47 $\mu\epsilon$/day), while 60 MPa concrete showed acceleration to 1.42 $\mu\epsilon$/day and 84 MPa to 0.80 $\mu\epsilon$/day, indicating non-linear strength dependence. Chamber exposure conditions amplified this effect in high-strength mixtures, with 60 and 84 MPa concretes showing dramatically faster development (+34% to +44% from 14 to 90 days), demonstrating that elevated temperature and low humidity significantly accelerate kinetics in denser mixes. Indoor exposure, however, demonstrated uniformly high development rates across all strengths (3.5–10.7$\times$ faster than outdoor), with 60 MPa achieving the greatest absolute increase (+378 $\times$ 10^{-6} $\mu\epsilon$ or $\approx$101%), suggesting that

50% RH conditions promote sustained moisture movement in intermediate-strength concretes despite their intermediate position in the strength spectrum.

The effectiveness of fiber reinforcement in mitigating shrinkage varied significantly across environmental conditions and development phases, correlating with the inherent shrinkage development rate. Under outdoor exposure (slowest development), steel fiber effectiveness demonstrated clear dosage dependence, with 0.5% SF reducing 90-day shrinkage by approximately −2% (23 MPa), −45% (40 MPa), −38% (60 MPa), and −23% (84 MPa), while 1.0% SF achieved greater reductions of −22% (23 MPa), −63% (40 MPa), −69% (60 MPa), and −34% (84 MPa). Under controlled chamber conditions (intermediate development), fiber performance showed more variable results, with 0.5% SF providing 25–24% reductions (23–84 MPa) and 1.0% SF achieving 34%, 11%, 8%, and 12% reductions for 23/40/60/84 MPa, respectively, indicating that fiber effectiveness diminishes for high-strength mixes under accelerated drying. In stark contrast, under indoor exposure (fastest development), steel fibers demonstrated superior mitigation capacity, with 0.5% SF reducing shrinkage by approximately 10%, 32%, 40%, and 20% for 23/40/60/84 MPa, and 1.0% SF achieving even stronger reductions, particularly for higher-strength concrete with 60 MPa shrinkage decreasing to 195.7 $\times$ 10^{-6} $\mu\epsilon$ ($\approx$74% reduction), demonstrating that fiber effectiveness is most pronounced under conditions with fastest development rates and highest absolute strain accumulation.

3.2. Drying Shrinkage Cracking

Cracking behavior was assessed through direct visual inspection and crack measurement. Outdoor and indoor specimens were inspected twice daily, while chamber specimens were examined only at the end due to environmental control constraints. Crack development was tracked regarding initiation time, width, length, and total area.

3.2.1. Cracking at Outdoor Exposure

The total cracking area serves as a critical indicator of the durability and serviceability of concrete under restrained conditions. As shown in Figure 6, the cracking area is highly sensitive to both the matrix compressive strength and the fiber reinforcement parameters (type and volume fraction). A primary observation across both fiber series is the significant increase in cracking area for the 60 MPa and 84 MPa mixes at lower fiber dosages. This trend is attributed to the high-performance nature of high-strength concrete, where lower water-to-cement ratios lead to a more refined pore structure, resulting in elevated capillary tension and intensified autogenous shrinkage [61,62]. In these dense matrices, the rapid accumulation of shrinkage stress often exceeds the early-age tensile capacity, leading to more pronounced macro-cracking when insufficient reinforcement is present [62,63].

In the Steel Fiber series, the cracking area was effectively suppressed to zero for the 23 MPa and 40 MPa mixes across all dosages (0.5% to 1.5%). However, for the 60 MPa and 84 MPa specimens, a clear dosage-dependent mitigation was observed. Specifically, in the 84 MPa mix, increasing the SF volume fraction from 0.5% to 1.5% resulted in a substantial reduction of the cracking area from approximately 28 to 12. The mechanical justification for this performance lies in the high elastic modulus (~200 GPa) and superior tensile strength of the steel fibers, which provide a robust “crack-bridging” mechanism [45,64]. These fibers act as internal micro-dowels that intercept crack tips at their inception, transferring stresses across the crack faces and arresting the crack opening. At higher dosages, the reduced spacing between fibers ensures a more continuous reinforcement network, which is essential for restraining the high-energy brittle fractures characteristic of high-strength cementitious matrices [65].

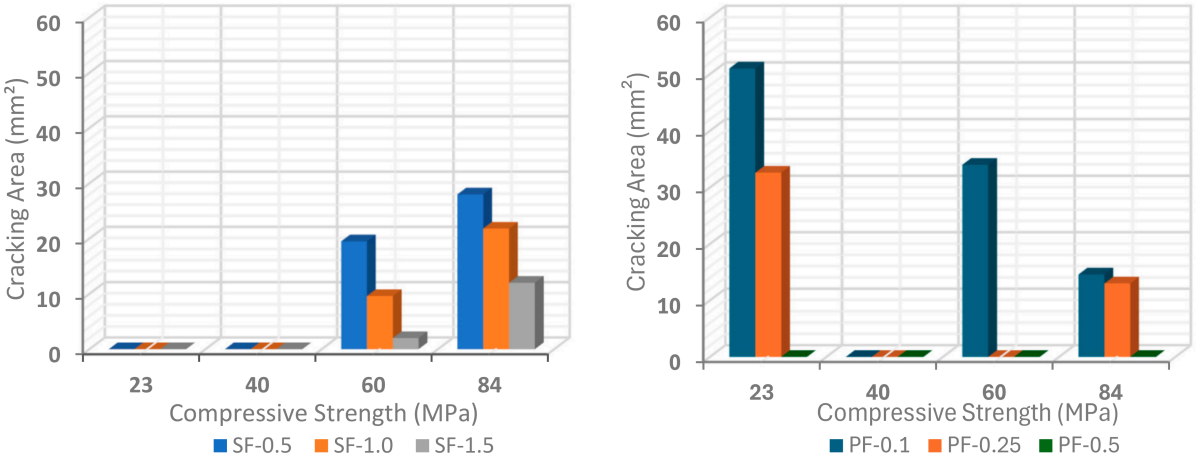


Figure 6. Cracking area of ring specimens exposed to outdoor conditions containing (**a**) steel fibers and (**b**) polypropylene fibers.

The Polypropylene Fiber series demonstrated a distinct mitigation profile, emphasizing the efficiency of synthetic fibers in controlling micro-scale deformations. At the 23 MPa strength level, the 0.1% PF dosage exhibited the highest overall cracking area (~52), likely due to the combination of a low-modulus matrix and an insufficient fiber volume fraction to resist initial desiccation stresses. However, increasing the PF dosage to 0.5% effectively eliminated measurable cracking across all strength grades (23–84 MPa). Unlike the rigid bridging provided by steel fibers, PF reinforcement operates through "stress dispersion," where the high count of fine filaments per unit volume ensures that shrinkage-induced stresses are uniformly distributed throughout the matrix rather than concentrating at potential crack sites. This mechanism prevents the coalescence of micro-cracks into macro-scale failures observed at lower dosage.

Comparing the two fiber types, the data suggests that while steel fibers are highly effective at limiting the width and area of macro-cracks in high-strength mixes (60–84 MPa), the polypropylene fibers at a 0.5% dosage offer a more comprehensive suppression of visible cracking across the entire strength spectrum. This is consistent with published findings indicating that low-modulus synthetic fibers are particularly adept at mitigating early-age plastic and drying shrinkage by improving the overall fracture toughness and reducing the brittleness of the composite [48,64]. In high-strength concrete where refined pore structures and rapid internal humidity drops generate extreme shrinkage stresses, these results indicate that a minimum fiber volume fraction (0.5% PF or 1.5% SF) must be utilized to prevent macro-cracking. Maintaining this crack-free integrity is vital for protecting the matrix from environmental ingress and ensuring prolonged service life [61].

3.2.2. Indoor Exposure

As illustrated in Figure 7, the cracking behavior under indoor laboratory conditions was characterized by a distinct relationship between concrete compressive strength and crack initiation. In the study, the plain concrete specimens exhibited delayed cracking compared to outdoor conditions, yet high-strength mixes remained significantly more vulnerable. Specifically, the 60 MPa plain concrete cracked as early as 3 days after exposure, while the 23 MPa, 40 MPa, and 84 MPa specimens cracked at 51, 26, and 22 days, respectively. The high susceptibility of the 60 MPa mix is consistent with its recorded strain profile, which showed the highest absolute shrinkage increase of approximately 101% between 14 and 90 days. This accelerated cracking in high-strength matrices is driven by the dense

pore structure and low water-cement ratio, which promotes rapid internal desiccation and the early buildup of tensile stresses.

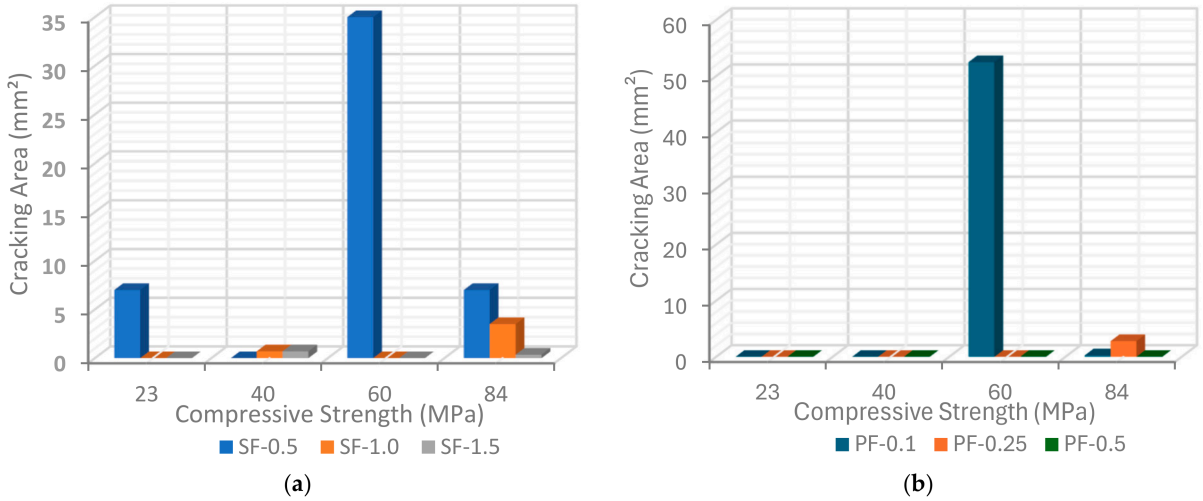


Figure 7. Cracking area of ring specimens exposed to indoor conditions containing (**a**) steel fibers and (**b**) polypropylene fibers.

The incorporation of fibers effectively mitigated these indoor cracking trends in a dosage-dependent manner, as shown in the subfigures of Figure 7. For the 60 MPa mix, which was the most prone to failure, a 1.0% Steel Fiber dosage or a 0.25% Polypropylene Fiber volume fraction was sufficient to prevent visible cracks entirely. In the 84 MPa concrete, which also presents a high risk of brittle failure, a higher 0.5% PF dosage was required to maintain a crack-free status. These results demonstrate that the optimization of fiber dosage is critical for high-performance concrete; while plain concrete suffers from singular macro-scale cracks, fiber reinforcement acts to bridge these crack planes and redistribute the tensile energy throughout the specimen. This reinforcement not only delays the age of first cracking but also significantly enhances the flexural toughness of the matrix, as reported in similar studies where fiber addition increased the toughness index by up to 7.7 times [15].

The distinct performance of the two fiber types in Figure 7 relates to their mechanical properties and interaction with the cementitious matrix. According to the material specifications, the Steel Fibers used (Modulus: 200 GPa) provide a robust macro-bridging mechanism that resists the substantial internal tensile stresses generated as drying progresses. By anchoring across crack faces, they prevent micro-cracks from coalescing into macro-cracks [64]. Conversely, the Polypropylene Fibers, characterized by their extremely fine diameter (0.034 mm) and high aspect ratio, function primarily by dispersing shrinkage-induced stresses at the micro-scale. This high filament count ensures that the fibers are distributed densely throughout the matrix, which significantly reduces stress concentrations. Literature indicates that this bridging effect can reduce measured shrinkage strain by approximately 15%, which aligns with the crack suppression observed in your 0.1% to 0.5% PF specimens [65]. Collectively, these findings underscore that while steel fibers provide superior resistance against macro-crack opening, polypropylene fibers offer a more efficient micro-reinforcement network for early-age crack prevention in indoor environments.

3.2.3. Control Exposure

Figure 8 presents cracking area measurements for ring specimens exposed to controlled-chamber conditions with an elevated temperature of 50 °C and a low relative humidity of 30%, representing severe drying exposure. Under these controlled, severe

conditions, the lower-strength grades (23 and 40 MPa) remained crack-free across all fiber types and dosages. This is attributed to the higher water-to-cement ratios and lower binder contents, which result in less intense drying shrinkage compared to high-strength mixes. However, as the matrix strength increased to 60 MPa and 84 MPa, the cracking area became significant, particularly at lower fiber volumes. The high susceptibility of these mixes is driven by the refined pore structure and rapid internal humidity drop, which generates extreme capillary tension and early-age tensile stresses.

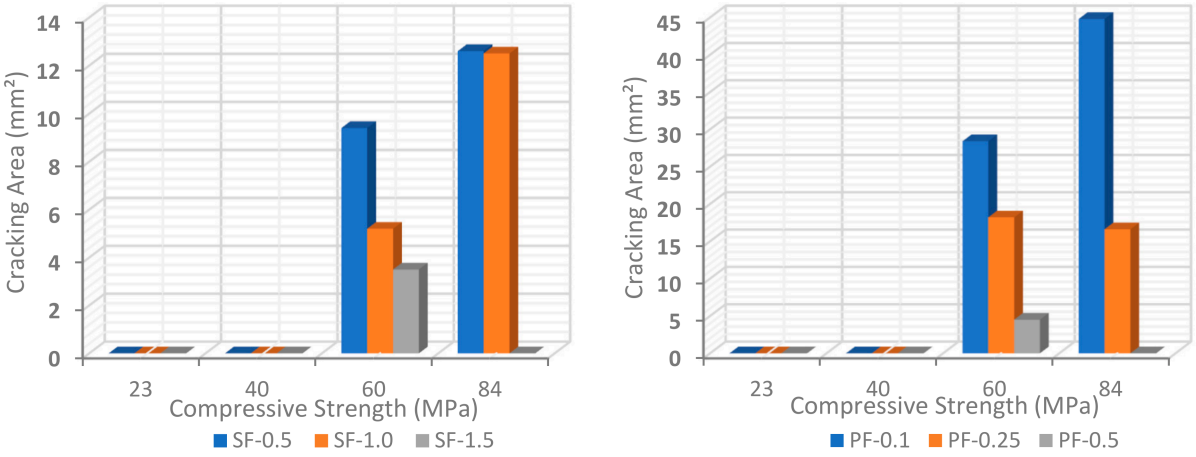


Figure 8. Cracking area of ring specimens exposed to control exposure conditions containing (**a**) steel fibers and (**b**) polypropylene fibers.

Both steel and polypropylene fiber inclusion demonstrated a capacity to reduce the total cracking area in the high-strength concretes exposed to the controlled chamber environment. In the steel fiber series (Figure 8a), the 60 MPa and 84 MPa specimens exhibited a clear dose-dependent reduction in cracking. For the 60 MPa mix, increasing the SF volume fraction from 0.5% to 1.5% reduced the cracking area from approximately 9.5 mm^2 to 3.5 mm^2. In the 84 MPa specimens, the cracking area remained relatively constant at 13 mm^2 for both 0.5% and 1.0% dosages, but was eliminated when the dosage reached 1.5%. This indicates that for high-strength matrices, a dosage of 1.5% SF is required to provide sufficient mechanical restraint to bridge the high-energy macro-cracks that form under restrained shrinkage. The steel fibers, with their high elastic modulus (~200 GPa), act as robust internal anchors that prevent the widening of cracks by transferring tensile loads across the fracture planes [64].

The polypropylene fiber series (Figure 8b) demonstrated higher initial cracking areas at the lowest dosage (0.1%) but achieved a "crack-free" status more efficiently at higher volumes. In the 84 MPa mix, the 0.1% PF dosage resulted in the largest observed cracking area of approximately 45 mm^2, nearly 3.5 times higher than the equivalent 0.5% SF specimen. However, as the PF dosage increased to 0.5%, the cracking area was reduced to zero across all strength grades. This suggests that while individual polypropylene fibers have a lower modulus, their high filament count per unit volume provides a superior stress-dispersion network.

The data in Figure 8 reveals a critical performance distinction: for the 84 MPa mix, 0.5% PF was more effective at achieving a crack-free state than 0.5% SF (which still exhibited 13 mm^2 of cracking). This suggests that in indoor conditions where drying is gradual but persistent, the high filament density of polypropylene fibers is more adept at arresting micro-cracks before they coalesce. Literature supports this, noting that fiber inclusion can reduce ultimate drying shrinkage strain by approximately 12.6% to 15%, thereby keeping

the accumulated tensile stress below the matrix's cracking threshold [65,66]. For long-term structural durability, these results underscore that high-strength concrete requires a minimum reinforcement level—specifically 1.5% SF or 0.5% PF—to guarantee the impermeable, crack-free integrity necessary for service in controlled indoor environments.

4. Conclusions

This research conducted a thorough experimental analysis of the drying shrinkage behavior in fiber-reinforced normal and high-strength concrete (23–84 MPa). It aimed to fill a significant gap in understanding how concrete strength, fiber type, and environmental exposure interact. The study involved 84 ring specimens tested under restrained conditions to assess how effectively steel and polypropylene fibers reduced shrinkage-related strain and cracking in three distinct settings: natural outdoor exposure, controlled indoor conditions, and an elevated-temperature-low-humidity chamber. The methodology adhered to ASTM C1581 for restrained ring testing, allowing for accurate tracking of strain development, crack initiation, width, and area. Based on the results, the study drew the following conclusions:

I. Restrained drying shrinkage strain increased with concrete compressive strength and environmental severity. High-strength concrete (60 and 84 MPa) consistently exhibited greater shrinkage and earlier cracking than normal-strength concrete.
II. Under outdoor exposure, plain 60 and 84 MPa concretes cracked within 2–6 days, while 23 MPa concrete showed no cracking throughout the test period.
III. Under indoor conditions (25 °C, 50% RH), 90-day shrinkage reached approximately 660×10^{-6} (23 MPa), 291×10^{-6} (40 MPa), 753×10^{-6} (60 MPa), and 338×10^{-6} (84 MPa), with the 60 MPa mix showing the highest long-term strain.
IV. Severe chamber exposure (50 °C, 30% RH) intensified shrinkage development in dense high-strength mixes and promoted cracking in 60 and 84 MPa concretes.
V. Steel fibers reduced shrinkage and cracking in a dosage-dependent manner; 1.0–1.5% steel fibers decreased 90-day shrinkage by up to 75% in 40–60 MPa concretes.
VI. Polypropylene fibers were highly efficient at lower dosages (0.25–0.5%), achieving shrinkage reductions up to 66% and eliminating cracking in several strength levels and exposure conditions.
VII. Fiber effectiveness depended on concrete strength and exposure condition, highlighting the need for technically effective fiber type and dosage selection for durability-oriented design under restrained drying environments.

This study confirms that drying shrinkage and cracking in concrete are primarily governed by strength level and environmental exposure, and that appropriately selected fiber type and dosage effectively enhance cracking resistance and long-term durability. Both steel and polypropylene fibers demonstrated technical efficacy in controlling shrinkage and cracking; however, a cost-effective analysis was not included in this scope. Future research should incorporate life-cycle cost analysis to develop economically informed fiber selection guidelines for practitioners. While shrinkage prediction model evaluation was initially considered, this investigation prioritized characterizing the fundamental mechanisms of fiber-reinforced concrete behavior under controlled ambient conditions. The experimental database of 84 restrained ring specimens tested across three distinct environmental exposures provides a rigorous empirical foundation for benchmarking and validating existing prediction models (ACI 209, B3, and CEB-FIP) in subsequent research. A comparative analysis of how current prediction models capture fiber-reinforcement and environmental interactions is recommended as a critical direction for future work.

Author Contributions: Conceptualization, T.A.S. and K.Z.F.; methodology, K.Z.F. and M.A.H.; validation, T.A.S. and K.Z.F.; investigation, M.A.H. and K.Z.F.; resources, T.A.S. and K.Z.F.; data curation, M.A.H.; writing—original draft preparation, M.A.H.; writing—review and editing, T.A.S. and K.Z.F.; supervision, T.A.S.; project administration, T.A.S. All authors have read and agreed to the published version of the manuscript.

Funding: This research received no external funding.

Data Availability Statement: The data presented in this study will be available on request from the corresponding author.

Acknowledgments: The author extended their appreciation to the Civil and Environmental Engineering Department, King Abdulaziz University, for their laboratory support. The authors also thank Polymerpave Global Corporation for providing the $CaCl_2$-blended acrylic polymer emulsion used in this study.

Conflicts of Interest: The authors declare no conflicts of interest.

References

1. Dhahir, M.K.; Marx, S. Shrinkage behaviour of high-strength concrete plates reinforced with carbon textile reinforcement. *Structures* **2024**, *69*, 107504. [CrossRef]
2. Yang, J.; Guo, Y.; Shen, A.; Wu, H.; Li, Y.; Lyu, Z.; Wang, W. Performance of basalt fibre reinforced concrete and resistance to shrinkage, cracking, and fatigue. *Int. J. Pavement Eng.* **2023**, *24*, 2141741. [CrossRef]
3. Alsaif, A.; Alharbi, Y.R. Strength, durability and shrinkage behaviours of steel fiber reinforced rubberized concrete. *Constr. Build. Mater.* **2022**, *345*, 128295. [CrossRef]
4. Yousefieh, N.; Joshaghani, A.; Hajibandeh, E.; Shekarchi, M. Influence of fibers on drying shrinkage in restrained concrete. *Constr. Build. Mater.* **2017**, *148*, 833–845. [CrossRef]
5. Yoo, D.Y.; Kim, S.; Kim, M.J. Comparative shrinkage behavior of ultra-high-performance fiber-reinforced concrete under ambient and heat curing conditions. *Constr. Build. Mater.* **2018**, *162*, 406–419. [CrossRef]
6. Afroughsabet, V.; Biolzi, L.; Ozbakkaloglu, T. High-performance fiber-reinforced concrete: A review. *J. Mater. Sci.* **2016**, *51*, 6517–6551. [CrossRef]
7. Afroughsabet, V.; Teng, S. Experiments on drying shrinkage and creep of high-performance hybrid-fiber-reinforced concrete. *Cem. Concr. Compos.* **2020**, *106*, 103481. [CrossRef]
8. Zieliński, A.; Schindler, A.K. Measurement of autogenous and drying shrinkage in paste, mortar, and concrete with the plastic-sleeve test method. *Mater. Struct.* **2025**, *58*, 246. [CrossRef]
9. Rasoolinejad, M.; Rahimi-Aghdam, S.; Bažant, Z.P. Prediction of autogenous shrinkage in concrete from material composition or strength calibrated by a large database, as update to model B4. *Mater. Struct.* **2019**, *52*, 33. [CrossRef]
10. Miao, Y.; Wang, H.; Zhang, Y.; Feng, T.; Yali, L.; Liqun, L.; Lin, J.; Zeyu, L.; Jiang, J. A numerical model for predicting the drying shrinkage behavior of concrete under ultra-low relative humidity. *Constr. Build. Mater.* **2024**, *411*, 134459. [CrossRef]
11. Ma, J.; Wang, T.; Wang, H.; Yu, Z.; Shen, X. A state-of-the-art review on the utilization of calcareous fillers in the alkali activated cement. *Constr. Build. Mater.* **2022**, *357*, 129348. [CrossRef]
12. Wang, L.; Tsang, D.C.W. Carbon dioxide sequestration on composites based on waste wood. In *Carbon Dioxide Sequestration in Cementitious Construction Materials*; Elsevier: Amsterdam, The Netherlands, 2018; pp. 431–450. [CrossRef]
13. Hwang, C.L.; Tran, V.A.; Hong, J.W.; Hsieh, Y.C. Effects of short coconut fiber on the mechanical properties, plastic cracking behavior, and impact resistance of cementitious composites. *Constr. Build. Mater.* **2016**, *127*, 984–992. [CrossRef]
14. Liu, L.; Wang, X.; Chen, H.; Wan, C. Microstructure-based modelling of drying shrinkage and microcracking of cement paste at high relative humidity. *Constr. Build. Mater.* **2016**, *126*, 410–425. [CrossRef]
15. Saradar, A.; Tahmouresi, B.; Mohseni, E.; Shadmani, A. Restrained Shrinkage Cracking of Fiber-Reinforced High-Strength Concrete. *Fibers* **2018**, *6*, 12. [CrossRef]
16. Abedi, M.; Kanstad, T.; Jacobsen, S.; Ji, G. Shrinkage properties of steel fiber reinforced concrete—A review. *Appl. Eng. Sci.* **2025**, *23*, 100244. [CrossRef]
17. Aghaee, K.; Khayat, K.H. Effect of shrinkage-mitigating materials on performance of fiber-reinforced concrete—An overview. *Constr. Build. Mater.* **2021**, *305*, 124586. [CrossRef]
18. Tran, N.P.; Gunasekara, C.; Law, D.W.; Houshyar, S.; Setunge, S.; Cwirzen, A. A critical review on drying shrinkage mitigation strategies in cement-based materials. *J. Build. Eng.* **2021**, *38*, 102210. [CrossRef]

19. Jafarifar, N.; Pilakoutas, K.; Bennett, T. Moisture transport and drying shrinkage properties of steel–fibre-reinforced-concrete. *Constr. Build. Mater.* **2014**, *73*, 41–50. [CrossRef]
20. Kassimi, F.; Khayat, K.H. Shrinkage of high-performance fiber-reinforced concrete with adapted rheology. *Constr. Build. Mater.* **2020**, *232*, 117234. [CrossRef]
21. Tabatabaeian, M.; Khaloo, A.; Joshaghani, A.; Hajibandeh, E. Experimental investigation on effects of hybrid fibers on rheological, mechanical, and durability properties of high-strength SCC. *Constr. Build. Mater.* **2017**, *147*, 497–509. [CrossRef]
22. Shatarat, N.; Katkhuda, H.; Abdel-Jaber, M.; Alqam, M. Experimental investigation of reinforced concrete beams with spiral reinforcement in shear. *Constr. Build. Mater.* **2016**, *125*, 585–594. [CrossRef]
23. Alberti, M.G.; Enfedaque, A.; Gálvez, J.C.; Agrawal, V. Fibre distribution and orientation of macro-synthetic polyolefin fibre reinforced concrete elements. *Constr. Build. Mater.* **2016**, *122*, 505–517. [CrossRef]
24. Hsie, M.; Tu, C.; Song, P.S. Mechanical properties of polypropylene hybrid fiber-reinforced concrete. *Mater. Sci. Eng. A* **2008**, *494*, 153–157. [CrossRef]
25. Kayali, O.; Haque, M.N.; Zhu, B. Some characteristics of high-strength fiber-reinforced lightweight aggregate concrete. *Cem. Concr. Compos.* **2003**, *25*, 207–213. [CrossRef]
26. Cao, M.; Zhang, C.; Lv, H. Mechanical response and shrinkage performance of cementitious composites with a new fiber hybridization. *Constr. Build. Mater.* **2014**, *57*, 45–52. [CrossRef]
27. Yoo, D.Y.; Park, J.J.; Kim, S.W.; Yoon, Y.S. Early age setting, shrinkage and tensile characteristics of ultra high performance fiber reinforced concrete. *Constr. Build. Mater.* **2013**, *41*, 427–438. [CrossRef]
28. Fraternali, F.; Ciancia, V.; Chechile, R.; Rizzano, G.; Feo, L.; Incarnato, L. Experimental study of the thermo-mechanical properties of recycled PET fiber-reinforced concrete. *Compos. Struct.* **2011**, *93*, 2368–2374. [CrossRef]
29. Radtke, F.K.F.; Simone, A.; Sluys, L.J. A computational model for failure analysis of fibre reinforced concrete with discrete treatment of fibres. *Eng. Fract. Mech.* **2010**, *77*, 597–620. [CrossRef]
30. Cho, C.G.; Kim, Y.Y.; Feo, L.; Hui, D. Cyclic responses of reinforced concrete composite columns strengthened in the plastic hinge region by HPFRC mortar. *Compos. Struct.* **2012**, *94*, 2246–2253. [CrossRef]
31. Olutoge, F.A.; Bhashya, V.; Ramesh, G.; Hanumantharai, B.; Sundar Kumar, S. Evaluation of residual strength properties of steel fiber reinforced concrete. *J. Emerg. Trends Eng. Appl. Sci.* **2013**, *4*, 168–172.
32. Kwon, S.H.; Shah, S.P. Prediction of Early-Age Cracking of Fiber-Reinforced Concrete due to Restrained Shrinkage. *ACI Mater. J.* **2008**, *105*, 381–389.
33. Kiviste, K.; Ryabchikov, A.; Lille, H. Determination of Shrinkage of Fibre Reinforced Concrete. *Civ. Eng.* **2011**, *11*, 113–116.
34. Zhao, S.; Li, C.; Zhao, M.; Zhang, X. Experimental Study on Autogenous and Drying Shrinkage of Steel Fiber Reinforced Lightweight-Aggregate Concrete. *Adv. Mater. Sci. Eng.* **2016**, *2016*, 2589383. [CrossRef]
35. Xiao, M.; Xu, N.; Hu, J.; Tang, Y.; Gao, P.; Li, F.; Wei, J.; Yu, Q. Quantification of coarse aggregate constraint on mortar shrinkage in concrete under drying condition. *Cem. Concr. Compos.* **2025**, *157*, 105876. [CrossRef]
36. Nasir, M.; Alimi, W.O.; Adeoluwa Oladapo, E.; Imran, M.; Kazmi, Z.A. Behavior of drying and plastic shrinkage of Portland cement concrete prepared and cured under harsh field. *Dev. Built Environ.* **2023**, *16*, 100252. [CrossRef]
37. Hu, X.; Shi, Z.; Shi, C.; Wu, Z.; Tong, B.; Ou, Z.; de Schutter, G. Drying shrinkage and cracking resistance of concrete made with ternary cementitious components. *Constr. Build. Mater.* **2017**, *149*, 406–415. [CrossRef]
38. Sivakumar, A.; Santhanam, M. A quantitative study on the plastic shrinkage cracking in high strength hybrid fibre reinforced concrete. *Cem. Concr. Compos.* **2007**, *29*, 575–581. [CrossRef]
39. Barr, B.; Hoseinian, S.B.; Beygi, M.A. Shrinkage of concrete stored in natural environments. *Cem. Concr. Compos.* **2003**, *25*, 19–29. [CrossRef]
40. Al Moman, A.; Sundar, D.; Zeng, K.; Tatar, J.; Radlińska, A.; Rajabipour, F. Autogenous and drying shrinkage in Ultra-High-Performance Concrete (UHPC) and the effectiveness of internal curing. *Constr. Build. Mater.* **2025**, *464*, 140217. [CrossRef]
41. Han, S.; Cui, Y.; Huang, H.; An, M.; Yu, Z. Effect of Curing Conditions on the Shrinkage of Ultra High-Performance Fiber-Reinforced Concrete. *Adv. Civ. Eng.* **2018**, *2018*, 5238278. [CrossRef]
42. Abdulridha, M.A.; Salman, M.M.; Banyhussan, Q.S. Effect Polypropylene of Fiber on Drying Shrinkage Cracking of Concrete Pavement Using Response Surface Methodology. *J. Eng. Sustain. Dev.* **2022**, *25*, 10–21. [CrossRef]
43. Kassimi, F.; Khayat, K.H. Flexural Creep and Recovery of Fiber-Reinforced SCC—Testing Methodology and Material Performance. *J. Adv. Concr. Technol.* **2021**, *19*, 67–81. [CrossRef]
44. Nassif, H.; Habib, M.; Obeidah, A.; Abed, M. Restrained Shrinkage of High-Performance Ready-Mix Concrete Reinforced with Low Volume Fraction of Hybrid Fibers. *Polymers* **2022**, *14*, 4934. [CrossRef]
45. *ASTM C1581*; Standard Test Method for Determining Age at Cracking and Induced Tensile Stress Characteristics of Mortar and Concrete Under Restrained Shrinkage. ASTM International: West Conshohocken, PA, USA, 2004. [CrossRef]
46. *ASTM C150*; Specification for Portland Cement [Internet]. ASTM International: West Conshohocken, PA, USA, 2020. Available online: http://www.astm.org/cgi-bin/resolver.cgi?C150C150M-20 (accessed on 10 March 2026). [CrossRef]

47. *ASTM C33/C33M-18*; Specifications for Concrete Aggregatess. ASTM International: West Conshohocken, PA, USA, 2018. [CrossRef]
48. *ASTM C16-03(2018)*; Test Method for Load Testing Refractory Shapes at High Temperatures. ASTM International: West Conshohocken, PA, USA, 2018. [CrossRef]
49. *ASTM C150/C150M-24*; Specification for Portland Cement. ASTM International: West Conshohocken, PA, USA, 2024. [CrossRef]
50. Murat Çebi, Y. Araştırma Makalesi Geleneksel ve Yüksek Dayanımlı Betonların Dayanımının İncelenmesi. *Rahva J. Tech. Soc. Stud.* **2024**, *4*, 57–68.
51. Hussein, H.H.; Rejeb, S.K.; Abd, H.T. Effect of Hybrid Fibers on the Mechanical Properties of High Strength Concrete. *Tikrit J. Eng. Sci.* **2014**, *21*, 10–18. [CrossRef]
52. Guo, Y.L.; Liu, X.Y.; Hu, Y.P. Study on the influence of fly ash and silica fume with different dosage on concrete strength. *E3S Web Conf.* **2021**, *237*, 03038. [CrossRef]
53. Zhang, J.; Li, H.; Zhao, Y.; Ren, G. An ontology-based approach supporting holistic structural design with the consideration of safety, environmental impact and cost. *Adv. Eng. Softw.* **2018**, *115*, 26–39. [CrossRef]
54. Tritsch, N.; Darwin, D.; Browning, J. *Evaluating Shrinkage and Cracking Behavior of Concrete Using Restrained Ring and Free Shrinkage Tests*; University of Kansas Center for Research, Inc.: Lawrence, KS, USA, 2005.
55. Menu, B.; Jolin, M.; Bissonnette, B. Assessing the Shrinkage Cracking Potential of Concrete Using Ring Specimens with Different Boundary Conditions. *Adv. Mater. Sci. Eng.* **2020**, *2020*, 4842369. [CrossRef]
56. Tian, C.; Zheng, Z.; Wei, X. The Dry Cracking of Cementitious Materials in the Eccentric Ring Test and the Concentric Ring Test. *J. Wuhan Univ. Technol.-Mater. Sci. Ed.* **2022**, *37*, 212–221. [CrossRef]
57. Prakash, R.; Divyah, N.; Selvapriya, V.; Mahakavi, P. Characterization and Image Processing Analysis on Polypropylene Fiber Reinforced Foamed Concrete. *Indian J. Sci. Technol.* **2024**, *17*, 333–342. [CrossRef]
58. Aziz, A.A.; Al-Mulla, I.F. Using the Schleibinger Test System to Study the Restrained Drying Shrinkage Behavior of Lightweight Concrete. *Eng. Technol. Appl. Sci. Res.* **2025**, *15*, 28018–28025. [CrossRef]
59. Sharda, S.; Singh, M.; Singh, S. A review on Properties of Fiber Reinforced Cement-based materials. *IOSR J. Mech. Civ. Eng.* **2016**, *13*, 104–112. [CrossRef]
60. Ding, D.; Zhang, L.; Zhao, J.; Li, C.; Wang, Z. Effects of air-entraining agent and polypropylene fiber on the mechanical properties, autogenous shrinkage, and fracture properties of fully recycled aggregate concrete. *Front. Mater.* **2022**, *9*, 1049304. [CrossRef]
61. Qin, J.; Gong, L.; Jin, C.; Dang, D.; Yang, T. Mechanism of shrinkage and cracking in high-strength concrete regulated by internal humidity under extreme drying environments. *Dev. Built Environ.* **2026**, *26*, 100902. [CrossRef]
62. Dong, W.; Zhou, X.; Wu, Z.; Xu, B. Investigating crack initiation and propagation of concrete in restrained shrinkage circular/elliptical ring test. *Mater. Struct.* **2017**, *50*, 73. [CrossRef]
63. Turcry, P.; Loukili, A.; Haidar, K.; Pijaudier-Cabot, G.; Belarbi, A. Cracking Tendency of Self-Compacting Concrete Subjected to Restrained Shrinkage: Experimental Study and Modeling. *J. Mater. Civ. Eng.* **2006**, *18*, 46–54. [CrossRef]
64. Gholami, M.; Moghadas Nejad, F.; Ramezanianpour, A.M. Increasing the Length of Concrete Pavement Slabs Using Shrinkage Reducing Admixture and Polypropylene Fiber. *Int. J. Concr. Struct. Mater.* **2023**, *18*, 9. [CrossRef]
65. Jin, Z.; Zhao, X.; Zhao, T.; Cao, Y. Effect of Mineral Admixture and Fibers on Shrinkage Crack of Sacrificial Concrete. *J. Adv. Concr. Technol.* **2016**, *14*, 502–510. [CrossRef]
66. Al-musawi, H.; Figueiredo, F.P.; Guadagnini, M.; Pilakoutas, K. Shrinkage properties of plain and recycled steel–fibre-reinforced rapid hardening mortars for repairs. *Constr. Build. Mater.* **2019**, *197*, 369–384. [CrossRef]

Disclaimer/Publisher's Note: The statements, opinions and data contained in all publications are solely those of the individual author(s) and contributor(s) and not of MDPI and/or the editor(s). MDPI and/or the editor(s) disclaim responsibility for any injury to people or property resulting from any ideas, methods, instructions or products referred to in the content.